Materials & Design 257 (2025) 114530

Contents lists available at ScienceDirect

Materials & Design

journal homepage: www.elsevier.com/locate/matdes

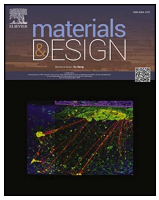

Prediction of recrystallization behavior during aluminum extrusion using physics-based modeling

Oliver Schulz [a,*], Lukas Kertsch [b], Johannes Gebhard [a], Yannis P. Korkolis [a], A. Erman Tekkaya [a], Maksim Zapara [b]

[a] Institute of Forming Technology and Lightweight Components (IUL), TU Dortmund University, Baroper Straße 303, 44227 Dortmund, Germany
[b] Fraunhofer Institute for Mechanics of Materials IWM, Wöhlerstraße 11, 79108 Freiburg, Germany

ARTICLE INFO

Keywords:
Hot extrusion
Microstructural prediction
6xxx alloys
Mean-field model

ABSTRACT

The mechanical properties of extruded aluminum profiles depend on the microstructure after extrusion. Prediction of the microstructure is therefore necessary, especially for the design of crash-relevant lightweight components. In this paper, the physics-based mean-field model developed by Fraunhofer IWM is originally introduced to aluminum extrusion to predict the recrystallization behavior during the hot extrusion of the aluminum alloys AA6060 and AA6082. A workflow consisting of material characterization, metallography, process simulation, and microstructural prediction for hot extrusion is established. The robustness and predictive capabilities of the calibrated model are validated on a double-chamber hollow profile extruded under standard industrial conditions. The mean-field model effectively predicts recrystallization based on plastic strain, strain-rate, and temperature evolution. The recrystallized areas of the hot extruded profiles could be predicted accurately. The grain size prediction of the directly quenched outer surfaces of the profile is relatively accurate (7 %), the maximum deviation of prediction and experimental observation is up to 52 %, depending on the location in the profile cross-section. With the successful calibration and validation for both alloys, the framework's versatility and the proposed workflow is demonstrated. Nonetheless, the results indicate that further investigations into input data sensitivity is necessary to further improve the model.

1. Introduction

Lightweighting strategies have been contributing to the reduction of material and energy requirements in various industrial sectors for many years. Extrusion is used as a particularly economical manufacturing process for the cost-efficient production of complex aluminum profiles. The mechanical properties of safety-relevant extruded components are particularly important. These profiles should have a continuously-controlled, high quality of microstructure (including spatial homogeneity of the microstructure, grain and subgrain size, recrystallized proportion of grains) in order to achieve consistent mechanical properties.

Plastic strain, strain-rate, and temperature across the cross-section of an extruded product are not uniform due to frictional effects and self-heating caused by plastic deformation as well as thermal and mechanical boundary conditions [1]. This results in microstructural variations both within the cross-section and in the longitudinal direction. A challenge is the formation of coarse grains in the areas near the surface of an extruded product due to the different local strain at the edge and in the center of the extrudate [2]. When the temperature, extrusion speed, and extrusion ratio are increased, dynamic recrystallization is promoted, resulting in a decrease of the grain size [3].

The kinetics of microstructural formation due to dynamic and static recovery as well as dynamic and static recrystallization are strongly influenced by the type and concentration of the alloying and accompanying elements dissolved in the solid solution, as well as by the distribution and type of primary and secondary precipitates [4].

To ensure satisfactory predictions of the microstructure, a precise characterization of the recrystallization phenomena is necessary to achieve suitable model parameters. However, no standard procedure for characterizing recrystallization under simplified conditions for different aluminum alloys is known in the literature. For AA7075 [5] and AA2024 [6], the achievable strains and strain-rates in a hot upsetting test were sufficient to achieve a recrystallized microstructure. Additionally, AA7050 could be characterized by hot tensile tests [7]. McQueen et al.

* Corresponding author.
E-mail address: oliver.schulz@iul.tu-dortmund.de (O. Schulz).

https://doi.org/10.1016/j.matdes.2025.114530
Received 14 May 2025; Received in revised form 14 July 2025; Accepted 5 August 2025
Available online 7 August 2025

[8] investigated the microstructural evolution of AA1070 under torsional load to achieve strains of up to 60. Güzel et al. [9] proposed a miniature extrusion press to characterize the dynamic recrystallization behavior of AA6082 under similar conditions as industrial extrusion. However, no dynamic recrystallization was observed for the investigated alloy composition and process parameters. It is understood that the alloying elements also influence the recrystallization behavior of a material [10,11]. For this reason, the limited strain-rates achievable under simplified conditions may not be sufficient to trigger recrystallization for some aluminum alloys.

There are currently different approaches to modeling the resulting microstructure, which can be referred to as empirical/phenomenological and physics-based models. For phenomenological approaches, the kinetics of recrystallization are described for example by the Johnson-Mehl-Avrami-Kolmogorov (JMAK) relationship, which calculates the volume fraction of the recrystallized material as a function of the hot forming conditions [12]. Pari and Misiolek [13] were able to include continuous and geometric dynamic recrystallization behavior in a combined model for a hot rolling process. This combination resulted in a good prediction of the recrystallization of AA6061. Furthermore, Foydl et al. [14] showed that a phenomenological model can be used to reproduce dynamic recrystallization in a good approximation to the experimental results. However, the determination of the material-specific set of model parameters requires a very large amount of data due to the high level of abstraction, which is why the prediction accuracy and the transferability of the calibrated models to changed process parameters or geometries is severely limited.

In recent years, new numerical approaches coupling crystal plasticity and recrystallization models were proposed. These approaches update grain population, crystal orientations, and dislocation densities in a crystal plasticity (CP) model, based on the microstructural evolution from a recrystallization model [15]. Manik et al. [16] were able to couple a crystal plasticity model with FEM for the prediction of the texture after extrusion of 6xxx alloys and achieved a good fit with the experimental results in the lower temperature regime. Another approach is the use of a viscoplastic self-consistent (VPSC) formulation coupled with finite element simulations (FE-VPSC). These models are able to predict the evolution of the texture in a spatially-varying strain field, as well as the anisotropy due to the microstructural evolution [17,18]. An adaptation of the field fluctuations viscoplastic self-consistent crystal plasticity model coupled with implicit finite element simulations (FE-FF-VPSC) was done, which was further able to predict the grain size distribution as well as including recrystallization by allowing the splitting of grains after reaching a critical value of the misorientation spread [19]. Traditionally, VPSC models did not explicitly account for grain size effects, although recent and more complex formulations [15] and [20] have been successfully developed to incorporate dynamic recrystallization phenomena. However, the industrial use of these models would require more extensive characterization than what is reported here, and longer computational times, both of which are oftentimes not desired.

Using the CALPHAD approach (**Cal**culation of **Ph**ase **D**iagrams), two different types of physics-based and thermodynamically-consistent models have been developed for several years [21]. The first type are mean-field-based models which are used to predict the evolution of precipitates, combining hardening, recovery and recrystallization effects [22], as well as predicting the grain size distributions [23]. Tzini and Haidemenopoulos included additional models to also consider the interaction of strain-induced precipitations and static recrystallization [24]. The second type are full-field-based models, such as cellular automaton models [25], level set and multi-phase-field method [26], or Monte Carlo models [27]. Due to their physical basis, these models require comparatively few model parameters [28] and are better suited for predictions over a large range of temperature and load (including extrapolation).

A mean-field modeling approach, utilizing thermodynamic principles to capture the coupling between the thermo-mechanical material behavior and the microstructural evolution, was initially developed by Kertsch and Helm [29] and subsequently finalized in Kertsch's PhD thesis [30]. The model enables the physical description and prediction of the behavior of precipitation-hardenable metals and alloys during cold and hot forming, as well as heat treatment. It captures phenomena such as work hardening, recovery, recrystallization and precipitation, as well as various coupling phenomena in a thermodynamically consistent manner, while offering rapid predictions due to its computationally-efficient mean-field approach.

Table 1 presents a comparison of the aforementioned microstructure modeling methods, while Table 2 compares the Kertsch-Helm approach with other core mean-field approaches. Due to its physical consistency, predictive power, and computational efficiency for industrial process simulations, the Kertsch-Helm mean-field modeling framework [29,30] is used in this paper and is applied to aluminum extrusion for the first time to calculate the recrystallization behavior during the forming process. The suitability and accuracy of the prediction is determined by industrial extrusion trials. To achieve this goal, sequential tasks have to be solved: initially the microstructural as well as the mechanical behavior of the investigated alloys are characterized by hot upsetting tests with a full factorial plan. The suitability of this test to achieve recrystallization under different conditions and alloys is further investigated. The model parameters are identified using a global stochastic optimization algorithm. To predict the microstructural changes during extrusion, the non-measurable state variables (strain-rate, temperature, pressure, stress) are calculated via FEM simulations and particle tracing. Lastly, the prediction results of the calibrated model are validated with laboratory- and industrial-scale extrusion trials.

2. Materials and methods

2.1. Workflow

The proposed workflow to achieve a satisfying microstructural prediction is shown in Fig. 1. The material flow curves as well as microstructural data (MS data), average grain size and recrystallization fraction, for different temperatures and strain-rates are determined with hot upsetting tests as an easy-to-control test method, and the material-dependent model parameters are calibrated. With the introduction of miniature extrusion trials, a first validation of the predicted average grain size and recrystallized fraction is performed with a minimized need for material. To fully predict the microstructure in extrusion processes, the evolution of the non-measurable state variables (e.g., temperature, pressure, strain-rate, and stress as functions of time) are calculated with finite element simulations (FEM). Finally, the precision and robustness are tested on an industry-relevant profile geometry and under industry standard conditions.

The microstructure model developed by Kertsch and Helm [29] and Kertsch [30] is used to calculate the evolution of the grain size distribution, the recrystallized fraction, and the yield stress from the history of temperature and plastic strain. All evolution equations are physics-based and derived from thermodynamic principles. A key strength of this model is its unified framework, where different recrystallization modes such as static, dynamic, and post-dynamic are not modeled separately but emerge naturally from a single set of physics-based equations depending on the thermomechanical history. For completeness, the model is reviewed below.

At each material point, the microstructure is described by a set of N spherical grains with radii $R_1, \cdots, R_N$. The hardening of grain i is modeled using the internal variables q_i^1 and q_i^2 describing the energy storage due to dislocations. Their definition and the corresponding evolution are motivated by a combination of dislocation density based and phenomenological plasticity models [30]. According to the Taylor assumption, all grains at a material point are subjected to the same deformation and temperature and the interaction of the grains is modeled using a mean-

Table 1
Comparison of numerical modelling methods to predict the microstructure.

Method	Computational Cost	Physical Detail	Industrial Applicability	Advantages	Limitations
Mean-field	Low	Moderate	Good	– Thermodynamic consistency – Fast computation – Multi-physics coupling	– Averaged spatial effects – Spherical grain assumption
Crystal Plasticity FEM	Very High	Very High	Limited	– Full spatial resolution – Complex geometries – Detailed mechanics	– Computationally prohibitive – Limited volume sizes
Advanced VPSC	Moderate	High	Good	– Texture evolution – Crystal mechanics – Size sensitivity	– Complex parametrization – Still homogenization-based
Cellular Automata	High	Moderate	Poor	– Spatial microstructure – Topological effects	– Mesh dependency – Phenomenological rules
Monte Carlo	Very High	Very High	Poor	– Fundamental physics – Stochastic effects	– Statistical convergence issues – Extreme computational cost

Table 2
Comparison of the Kertsch-Helm modelling framework with other core mean-field approaches.

Aspect	Kertsch-Helm [29,30]	Hillert [31]	Fischer-Svoboda [32]	Cram et al. [33]	Bernard et al. [34]	Riedel-Svoboda [22]
Thermodynamic Foundation	Müller-Liu consistent	Energy-based only	Onsager extremal principle	Energy-based	Energy + grain boundary terms	Chaboche-type phenomenological
Energy Conservation	Rigorous enforcement	Approximate	Extremal principle based	Not enforced	Partial	Not addressed
Parameter Physics	Physically meaningful	Simple geometric	Thermodynamic + kinetic	Mixed physical/ empirical	Mixed physical/ empirical	Largely empirical
Multi-physics Coupling	Native unified framework	Grain growth only	Precipitation focus	Mechanical only	Mechanical + thermal	Limited coupling
Computational Efficiency	High	High	Moderate	High	Moderate	Low

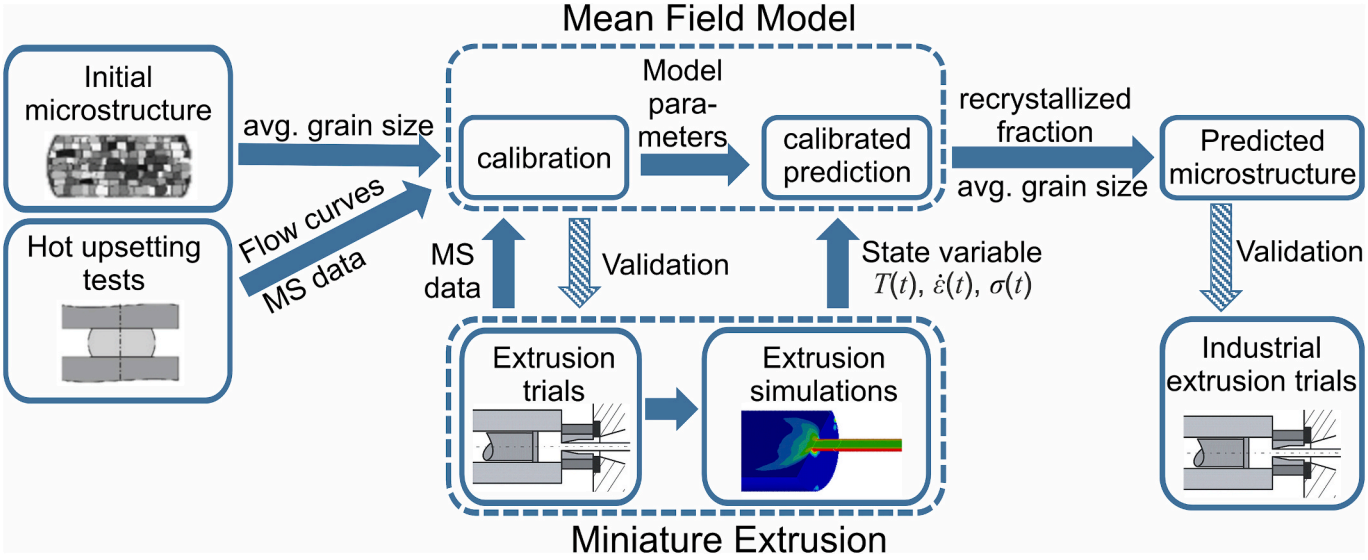

Fig. 1. Workflow for the prediction of the microstructure with a mean-field-model (MS: Microstructural data).

field approach. The grain sizes evolve according to

$$\dot{R}_i = -M_{\mathrm{gb}}\left(\psi_{\mathrm{p},i} + \frac{\sigma_{\mathrm{gb}}}{R_i} + \Lambda\right)(i = 1, \cdots N) \tag{1}$$

where $M_{\mathrm{gb}}(T)$ denotes the temperature-dependent grain boundary mobility following Arrhenius kinetics for thermally activated processes with M_0 the pre-exponential factor, Q_{gb} the grain boundary migration activation energy, R the gas constant (8.314 J/(mol·K)) and T the absolute temperature.

$$M_{gb}(T) = M_0 \cdot \exp\left(\frac{-Q_{gb}}{R \cdot T}\right) \tag{2}$$

The terms in the parenthesis of Eq (1) are the driving pressures with units of energy density [J/m^3] with σ_{gb} the grain boundary energy per unit area, $\psi_{\mathrm{p},i}$ the stored energy due to plastic deformation of the i-th grain and Λ the Lagrange multiplier. This energy storage is expressed by

$$\psi_{\mathrm{p},i} = \mu \sum_{j=1}^{2} \xi^j \left(q_i^j\right)^2 / 2 \tag{3}$$

with the temperature-dependent shear modulus $\mu(T)$ and constant pa-

rameters ξ^j, which in turn are functions of the two internal variables q_i^j. The Lagrange multiplier Λ in Eq. (1) ensures volume conservation and is calculated from the condition

$$\sum_{i=1}^{N} R_i^2 \dot{R}_i = 0 \tag{4}$$

Recrystallization is modelled by the fact that a grain i produces new recrystallized grains with the nucleation rate

$$\dot{N}_i = A\left[1+\varphi_1\left(\frac{\dot{\varepsilon}_p}{\dot{\varepsilon}_0}\right)^{\varphi_2}\right] R_i^2 \langle \psi_{p,i} - \psi_{p,cr} \rangle \tag{5}$$

In Eq. (5), $\psi_{p,cr}(T)$ represents the critical plastic energy. Nucleation occurs only in grains whose plastic energy exceeds this threshold. This behavior is modeled by the Macauley brackets $\langle\rangle$ defined by $\langle x \rangle = (x+|x|)/2$. The variables $A(T)$, $\varphi_1(T)$, $\varphi_2(T)$, and $\dot{\varepsilon}_0 = 1\,\mathrm{s}^{-1}$ are further model parameters, and $\dot{\varepsilon}_p$ denotes the equivalent plastic strain-rate. Recrystallized grains initially have the very small size R_0 and can grow according to Eq. (1). The evolution of the hardening variables is described by the equation

$$\dot{q}_i^j = \left[1-\beta^j\left(\frac{\dot{\varepsilon}_p}{\dot{\varepsilon}_0}\right)^{-x^j} q_i^j\right]\dot{\varepsilon}_p - \alpha^j q_i^j - 3\langle\frac{\dot{R}_i}{R_i}\rangle q_i^j (i=1,\cdots N, j=1,2) \tag{6}$$

where the parameters $\beta^j(T)$ and x^j control dynamic recovery and $\alpha^j(T)$ controls static recovery. The last term in Eq. (6) is related to the softening due to the growth of recrystallized grains. Finally, the yield stress is calculated by

$$\sigma_y = k_0 + \mu \sum_{i=1}^{N} z_i \left[\sum_{j=1}^{2} \xi^j q_i^j\right] \tag{7}$$

where $k_0(T)$ denotes the temperature-dependent intrinsic strength and $z_i = R_i^3 / \sum_{j=1}^{N} R_j^3$ the volume fraction of the i-th grain on the polycrystalline ensemble. However, the calculated yield stress is not used in the FEM, since the calculation is only run as a post processing tool to save computational cost.

2.2. Materials and specimen preparation

The two aluminum alloys AA6060 and AA6082 are selected due to their high technological and economic importance for extrusion processes. The alloys are produced according to the European standard for wrought aluminum (EN AW) and are obtained as billets with a diameter of 203.2 mm in a homogenized state. Their chemical composition is provided by the manufacturer by spectral analysis and is listed in Table 3. The composition of the AA6082 alloy show a rather low amount of silicon (0.7 – 1.3), manganese (0.4 – 1.0) and magnesium (0.6 – 1.2) compared to the range of such an alloy. Especially due to the rather low amount of magnesium, a more pronounced recrystallization behavior is to be expected compared to a more average 6082 alloy.

The specimens for the hot upsetting tests and miniature extrusion trials are cut with a water jet to avoid heating effects and any change in the initial microstructure. The specimens for hot upsetting have a diameter of 10 mm and a height of 15 mm, whereas the miniature extrusion billets have a diameter of 19 mm and a height of 25 mm. The cylindrical specimens are cut out in a grid across the cross section of the billet. Due to the homogenized state, in which the billets arrived, a homogeneous average grain size is observed over the initial cross section. Therefore, the position of the specimen does not influence the initial grain size for further investigations.

2.3. Hot upsetting

The isothermal hot upsetting tests to determine the flow curves, model parameters and microstructural evolution are carried out on a Gleeble 3150 thermomechanical testing machine under closed-loop control to maintain isothermal conditions and constant true strain-rates until barreling of the sample. In this work, the samples are loaded further to investigate the recrystallization behavior. The temperature was consistently measured and remained constant due to the relatively short process time. The setup (Fig. 2) includes a pneumatic ejector and a water quench for targeted and immediate quenching of the deformed samples. To reduce friction and ensure good electrical conductivity, both ends of the samples are prepared with nickel paste and graphite foil. A camera setup and several thermocouples are also used to monitor the deformation behavior and temperature of the samples. For the calibration of the material parameters, only data from the stable deformation regime of the upsetting tests were used.

2.4. Miniature extrusion

A self-developed miniature extrusion press [9] is used to perform the extrusion trials for initial validation of the predicted microstructure, as well as the characterization of the recrystallization behavior of AA6082.

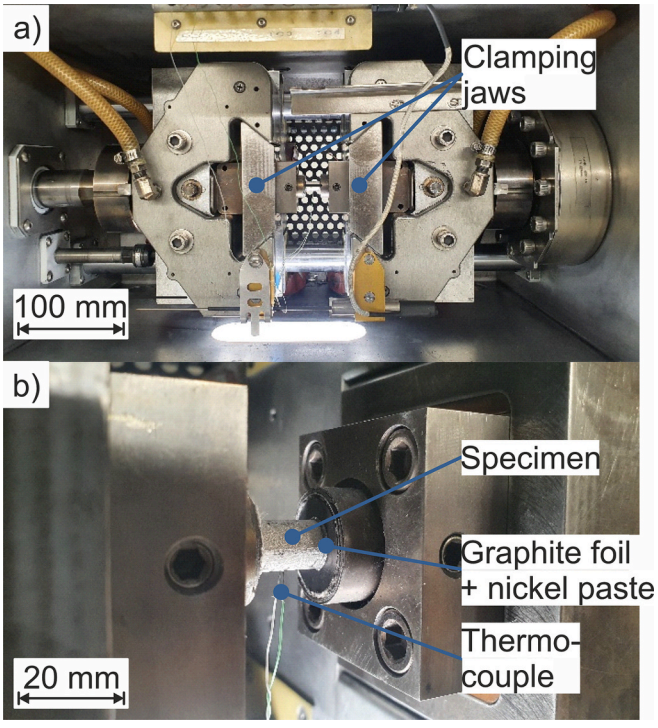

Fig. 2. a) experimental setup for the hot upsetting tests on the Gleeble 3150 with an additional water quench below the clamping jaws (not pictured here), b) thermocouple on the specimen to monitor the temperature during testing.

Table 3
Chemical composition of the used aluminum alloys.

	Si	Fe	Cu	Mn	Mg	Cr	Ni	Zn	Ti	Ga	V	B	Zr
AA6060	0.524	0.217	0.003	0.046	0.472	0.002	–	0.016	0.011	–	–	–	–
AA6082	0.870	0.120	0.018	0.420	0.730	0.010	0.004	0.012	0.028	0.008	0.007	0.001	0.002

The setup is shown in Fig. 3, which includes additional thermocouples in the die and the punch to measure the temperature evolution in these areas and investigate the influence on the recrystallization and recovery mechanisms. The recipient, die, and billet are heated to the desired temperature in an external furnace, which ensures that all three have the same temperature at the beginning of the test. A water-filled tube below the recipient is integrated to immediately quench the extruded profile and freeze the microstructure in the state after forming. The discard, die, and recipient can be quenched in an additional water bath in front of the test setup, which allows analyzing the highly inhomogeneous microstructure in the discard. The water in both containers is replaced after each test to avoid heating. The parameters for the extrusion trials are given in Table 4.

2.5. Microstructure analysis

For the analysis of the microstructure, the specimens are cold mounted, electrolytically etched using the Barker's reagent, and investigated with optical microscopy under polarized light. Due to the large number of different investigated specimens and the possibility to time-efficiently analyze the complete cross-section, light microscopy was chosen as a reasonable method to assure quantification of the microstructure analysis. The grain size is determined as an average grain length l_{ag} with the mean linear intercept method in accordance with ISO 643. To compare the measured grain sizes with the predictions of the microstructure model, an equivalent three-dimensional grain diameter $\overline{D}$ is calculated by $\overline{D} = 1.5 \cdot l_{ag}$ [35].

2.6. Numerical determination of non-measurable process parameters

To expand the experimental database with the non-measurable state variables such as pressure, stress, temperature and strain-rate, numerical process simulation of the miniature extrusion trials are conducted with the FEM program Inspire Extrude Metal from Altair. The steady-state regime based on the Euler approach is modeled with the flow volume extracted from the die and container model of the experimental setup. With the definition of the bearing zone on the die, the resulting profile is also generated. The complete model is discretized with 1st order tetrahedral elements with 4 nodes TET4 in Inspire Extrude by Altair with a total element count of 67,432 ($R = 25$), 72,898 ($R = 44$) and 1,126,811 (AA6082) for the simulation of miniature extrusion and 2,754,763 while using symmetry and only modeling a quarter of the process for the industrial extrusion. Due to the Eulerian conditions of the mesh, for a minimum element length in the bearing area of 0.35 mm, 0.175 mm or

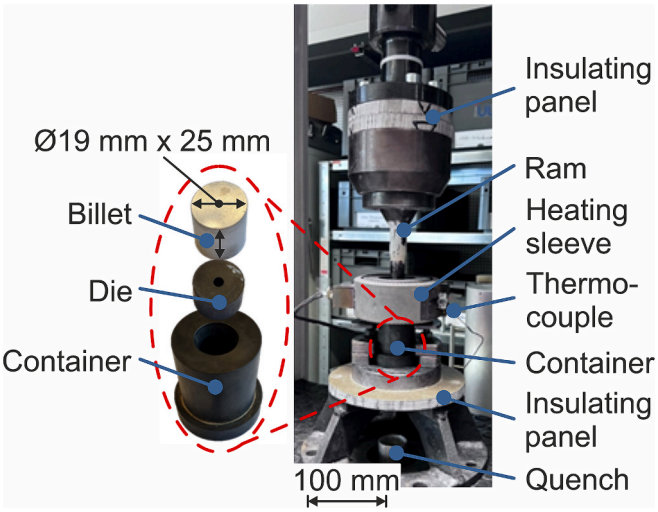

Fig. 3. Setup of the miniature extrusion press [9].

Table 4
Parameters for the miniature extrusion trials.

Extrusion ratio R	Ram speed v_{ram} (mm/s)	Temperature T (°C)
11.11	5	420 (only for AA6060)
25	9	450 (only for AA6082)
44.44		550
		600

0.05 mm the maximum calculated strain, strain-rate and temperature did not change. However, the relatively fine discretization is necessary to distinguish between multiple particle traces. The plastic behavior of the workpiece was modelled with the Zener and Hollomon model [36] modified by Sellars and Tegart [37], with parameters obtained from the program's database. The present model for AA6060 is in good agreement with the flow curves presented in the next section (see **A.1**). The investigated flow curves of AA6082 (**Section 3.1**) show in average an 11 % higher flow stress compared to the ones found in the program's database. Therefore, the predefined material model was scaled accordingly: $\sigma_f = 10/9 \bullet \sigma_{f,Model}$. Additionally, two different friction models are used. On the container and die wall, sticking friction is assumed. Along the bearing zone both sticking and slipping conditions apply [38]. Therefore a viscoplastic friction model, which includes the shear stress as a function of pressure and flow stress, with a friction coefficient of $\mu = 0.3$ is used, which resulted in a similar maximum ram force compared to the experimental trials as well as providing good results in the literature [39]. The process parameters are set according to the values of the investigated experiments. The numerical calculated stationary ram force represents the maximum force in the respective force–displacement curves from the experiments which are used for validation, see **A.2**.

In order to understand the evolution of the microstructure, the state variables are computed along selected paths (Fig. 4). For this purpose, individual material points, referred to as particles, are defined on the cross section of the extruded profile and followed backwards throughout the extrusion process.

3. Results and analysis

3.1. Flow curves

Hot upsetting tests, as described in **Section 2.3**, are conducted to determine the material flow curves under strain-rates of 0.1 to 3 s^{-1}. Plastic strains up to 1.5 are successfully tested and isothermal conditions are ensured during the test. Each test condition is repeated to ensure reliability. With a standard deviation for the measured flow stress in the range of 1–3 MPa, or approximately ±2–6 % of the absolute stress value, the experimental scatter between the repeated tests is low, reflecting the high fidelity of the Gleeble equipment. The curves shown in Fig. 5 and Fig. 6 represent arithmetic mean values of the floe stresses measured in the repeated tests.

The flow curves determined for AA6060 show a clear strain-rate dependence (Fig. 5), i.e., the yield stress increases with increasing strain-rate. In contrast, the stresses at 550 °C are considerably lower

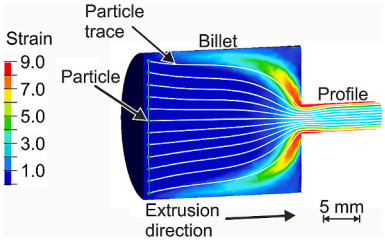

Fig. 4. Exemplary 3D process simulation with particle trace calculation to determine the evolution of the state variables. A symmetric cut is introduced to visualize the particle paths inside the die.

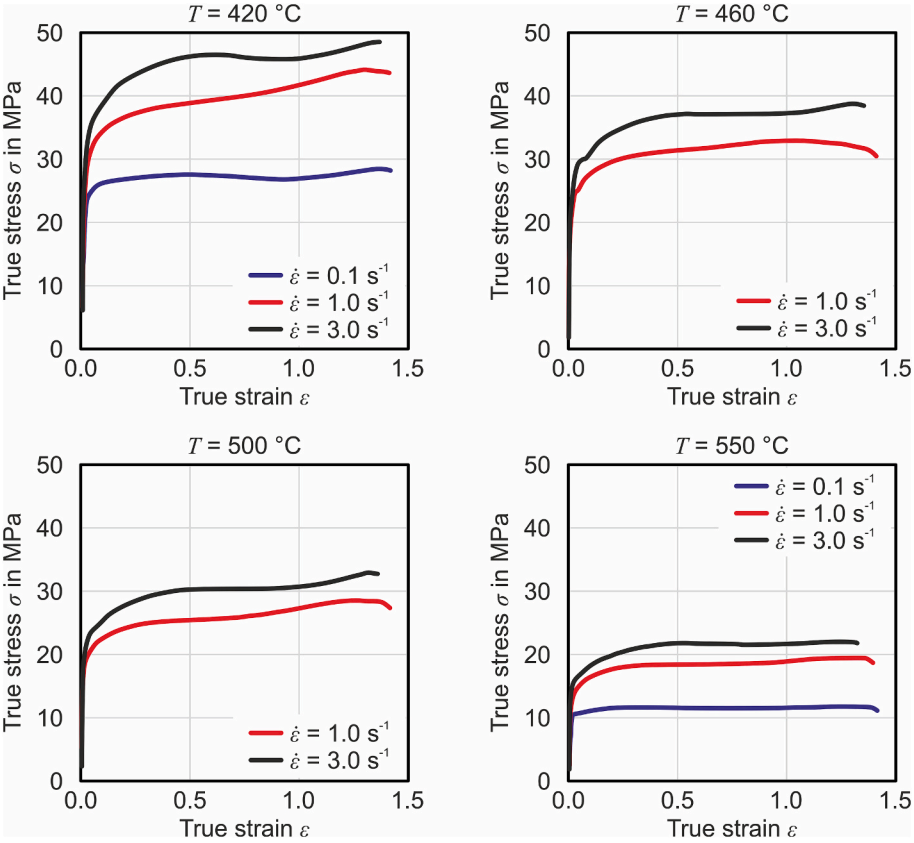

Fig. 5. Temperature and strain-rate dependent flow curves determined by hot upsetting tests of AA6060.

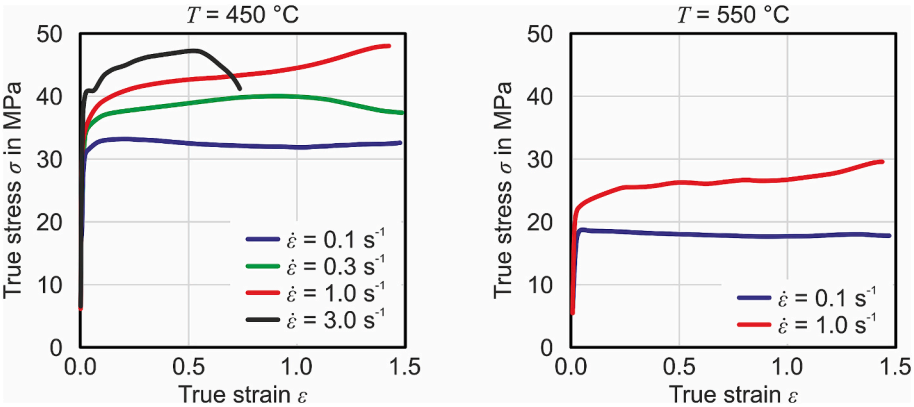

Fig. 6. Temperature and strain-rate dependent flow curves determined by hot upsetting tests of AA6082.

than at 420 °C. After a steep initial increase, all flow curves are very flat. It should be noted that at higher deformation speeds, the specified strain-rate was only achieved at higher strain. Corrected for this effect, these flow curves would be even flatter. This shows that, as a result of pronounced dynamic recovery, the material exhibits only weak work-hardening. The flow curves show no softening behavior and therefore no signs of dynamic recrystallization.

Similar temperature and strain-rate dependencies like for AA6060 can be seen in the flow curves of AA6082 (Fig. 6). This alloy also shows a pronounced dynamic recovery and no signs of dynamic recrystallization. The fact that the flow stress at 450 °C and a nominal strain-rate of 3 s^{-1} seems to drop after a strain of 0.5 can be explained by a drop of the actual strain-rate. In general, friction effects and other perturbations increase at higher strains, such that the flow curves should not be interpreted at strains of more than approx. 1.

3.2. Microstructural evolution during hot upsetting experiments

The microstructural evolution during hot upsetting is investigated for different combinations of the process parameters billet temperature T_B, strain-rate $\dot{\varepsilon}$, total strain ε_t, and holding time t after deformation. However, since a strain-rate of more than 3 s^{-1} cannot be controlled constantly due to the acceleration process of the machine crosshead, only strain-rates up to 1 s^{-1} are considered. To investigate the static and dynamic recrystallization behavior, the samples are either quenched immediately, or kept at the test temperature for a defined additional period of maximum t = 30 s after forming. The temperature range investigated corresponds to the usual temperatures during extrusion, ranging from 420 °C to 550 °C.

Using the optical microscopy, no dynamic recrystallization can be determined for either alloy (Fig. 7a, b), which is consistent with the

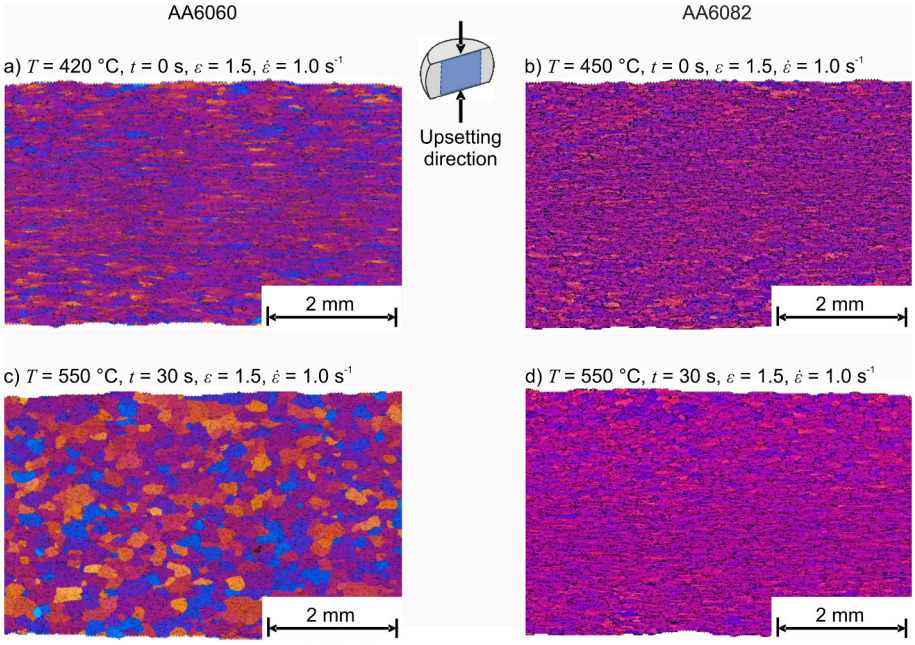

Fig. 7. Resulting exemplary microstructures after the hot upsetting with direct quenching, showing no recrystallization for both alloys (a and b), and delayed quenching resulting in recrystallization only for AA6060 (c) and not AA6082 (d). The blue box in the schematic is of the same size as the micrographs.

observed flow curves. A completely statically recrystallized microstructure of AA6060 could only be achieved by increasing the time between upsetting and quenching of the specimen (Fig. 7c). For AA6082, no nucleation or recrystallization is observed for any of the parameters tested, even with a delay between upsetting and quenching (Fig. 7d). As already analyzed in the literature [10,11], the significantly higher manganese content (0.42 wt% compared to ≤0.1 wt% for AA6060) hinders grain boundary motion and causes the formation of dispersoids, which actively hinder recrystallization of the microstructure due to the increased Zener drag [10], and would therefore need higher strains to achieve the onset of recrystallization.

The resulting average grain length of the recrystallized microstructure of AA6060 could be varied via the process parameters and is between 105.2 µm (T_B = 460 °C, ε_t = 1.5, t = 30 s) and 217.11 µm (T_B = 550 °C, ε_t = 0.8, t = 30 s) (Fig. 8). Below a block temperature of 460 °C, only a compression of the grain structure is observed, but no nucleation. For comparison, in the initial homogenized state, the average grain length is 97.34 µm and 93.40 µm for AA6060 and AA6082, respectively.

Due to the absence of recrystallization in the upsetting tests of AA6082, additional test methods to achieve recrystallization are needed for the calibration of the microstructure model; however, for AA6060 the hot upsetting tests are sufficient for the calibration.

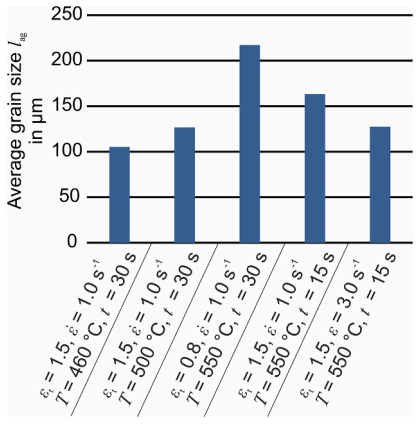

Fig. 8. Average grain size after hot upsetting of AA6060 for an exemplary selection of process parameters.

3.3. Calibration of the microstructural evolution model for AA6060 using hot upsetting

The parameters of the microstructural evolution model are calibrated using a two-step procedure. At first, the parameters controlling the intrinsic strength, hardening, and recovery phenomena, i.e., those from the equations (6) and (7), are identified based on the flow curves from the hot upsetting tests using a global stochastic optimization algorithm, specifically the differential evolution algorithm. As Fig. 9 shows that for AA6060, the measured and calculated flow curves match very well and the temperature and strain-rate dependencies are accurately reproduced.

Equation (3) shows that the hardening serves furthermore as a driving force for recrystallization. Therefore, the model parameters from the equations (1) and (5) describing the recrystallization behavior are identified in a second step, using the already calibrated plasticity parameters. Due to the interaction of the model equations, this part of the parameter identification is performed with a heuristic approach using the observed microstructural evolution in the upsetting tests. The calibrated model parameters for AA6060 are given in Table 5. It should be noted that the grain boundary energy σ_{gb} has been set to zero. This was necessary, because the calculated driving forces for recrystallization are relatively low compared to the capillarity forces resulting from the more realistic value of σ_{gb} = 0.324 J/m^2 [40]. Since the parameter σ_{gb} has no influence on the static recrystallization behavior and is mainly relevant in grain coarsening when no deformation is involved, this choice may be acceptable in this application, where recrystallization is driven by the stored energy due to plastic deformation. However, a more realistic value of σ_{gb} should be used in future work. For this, it may be necessary to adjust the parameters related to work hardening in order to achieve a more suitable plastic energy level compared to the grain boundary energy.

Fig. 10 shows exemplarily the calculated recrystallization behavior (solid line) and experimental results (square symbol) at 550 °C in terms of the recrystallized fraction (Fig. 10a and c) and average grain size (Fig. 10b and d) for total strains of ε_t = 0.8 and 1.5, as well as two

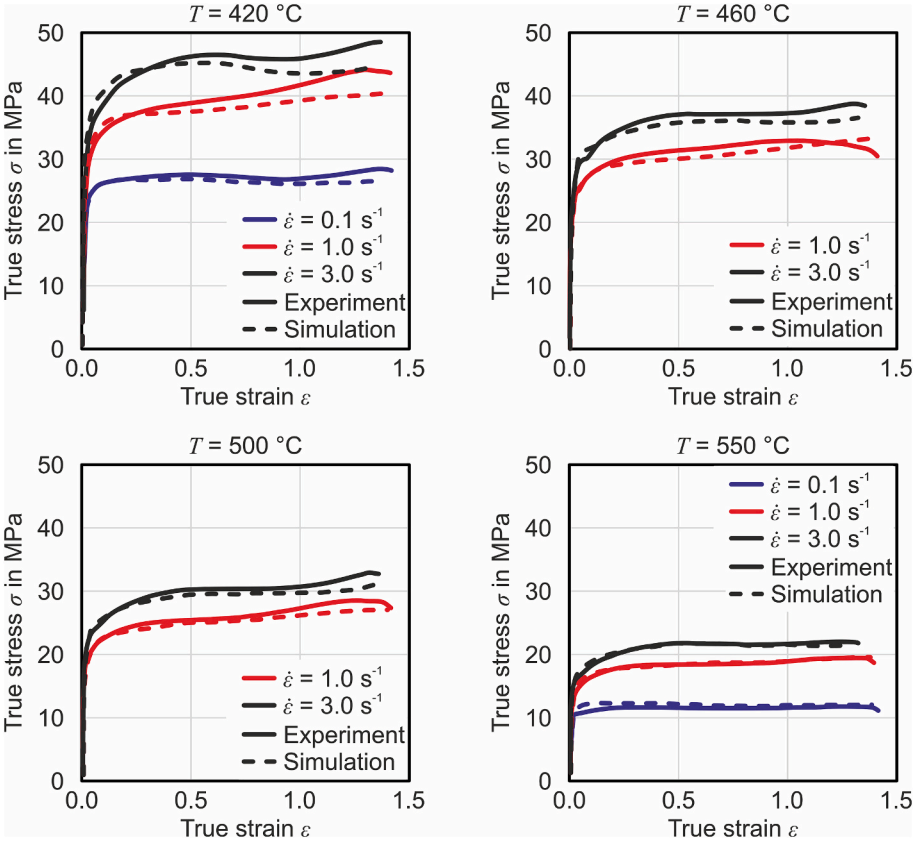

Fig. 9. Temperature and strain-rate dependent flow curves of AA6060 calculated with the mean-field microstructure model and compared with the experimentally determined flow curves using hot upsetting test.

Table 5
Parameters of the microstructural evolution model for AA6060. R_{gas} denotes the gas constant and T the absolute temperature.

	AA6060
μ in GPa	$26\left(1-0.2\frac{T-300\,\mathrm{K}}{600\,\mathrm{K}}\right)$
ξ^1	0.0167
β^1	$2622.75\exp\left(-\frac{25\,\mathrm{kJ/mol{\cdot}K}}{R_{gas}\cdot T}\right)$
x^1	0.1077
ξ^2	0.9087
β^2	$24625.9\exp\left(-\frac{19\,\mathrm{kJ/mol{\cdot}K}}{R_{gas}\cdot T}\right)$
x^2	0.2243
$a^1 = a^2$ in s^{-1}	$0.5\exp\left(-\frac{25\,\mathrm{kJ/mol{\cdot}K}}{R_{gas}\cdot T}\right)$
M_{gb} in $\frac{\mathrm{m}^4}{\mathrm{J\bullet s}}$	$1.5{\cdot}10^{-5}\exp\left(-\frac{65\,\mathrm{kJ/mol{\cdot}K}}{R_{gas}\cdot T}\right)$
σ_{gb} in $\frac{\mathrm{J}}{\mathrm{m}^2}$	0
A in s^{-1}	$10^{15}\exp\left(-\frac{118\,\mathrm{kJ/mol{\cdot}K}}{R_{gas}\cdot T}\right)$
φ_1	0
φ_2	1
$\psi_{p,cr}$ in $\frac{\mathrm{J}}{\mathrm{m}^3}$	$2.3{\cdot}10^8\left(1+\tanh\left(20.32-0.0343\frac{T}{\mathrm{K}}\right)\right)+4.1{\cdot}10^4$
R_0 in µm	1
k_0 in MPa	$5.64\left(1-0.78\frac{T-693\,\mathrm{K}}{130\,\mathrm{K}}\right)$

holding times $t = 15$ s and 30 s. As expected, increasing the strain results in a faster recrystallization, as the higher dislocation density leads to a higher driving force. As recrystallization sets in, the calculated average grain size drops due to the formation of new small grains. As the nuclei grow and hence consume the deformed grains, the average grain size increases again. The calculated final grain sizes are in good agreement with the measured values. Also at lower temperatures, the model reproduces the observed recrystallization behavior. At 420 °C, the model predicts that no recrystallization occurs in the upsetting tests, which is in accordance with the experimental observation as shown in Section 3.2.

Even though the mean-field model does not directly incorporate the influence of the different alloying elements on the effect of recrystallization, such as Manganese (as stated in Section 3.2), the model implicitly accounts for compositional differences through the calibration of material-specific parameters, such as the grain boundary mobility M_{gb} and the critical energy for nucleation $\psi_{p,cr}$, which are fitted to the macroscopic behavior of each specific alloy.

3.4. Lab-scale validation and analysis of the model behavior for AA6060

Miniature extrusion trials are performed on AA6060, in order to validate the predicted microstructure of the calibrated model. To further investigate the robustness of the model, multiple combinations of different process parameters (extrusion ratio R, billet temperature T and ram speed v_{ram}) are tested out to achieve different resulting microstructures. The same temperature as for the upsetting tests, with an additional homogenization of the billets for 30 min before extrusion, and standard extrusion ratios for the industry between $R = 11.11$ and $R = 44.44$ are investigated.

In contrast to the hot upsetting test, the miniature extrusion trials show a recrystallization of the microstructure for all inspected parameter combinations of AA6060 due to the higher plastic strain-rates $\dot{\varepsilon}_{eq}$, especially on the profile outer edges (up to $\dot{\varepsilon}_{eq} = 500\ \mathrm{s}^{-1}$). The extruded microstructure on three positions along the extruded length is shown in Fig. 11. The beginning of the profiles show a homogeneous microstructure along the extrusion axis (b-c and e-f). With decreasing distance

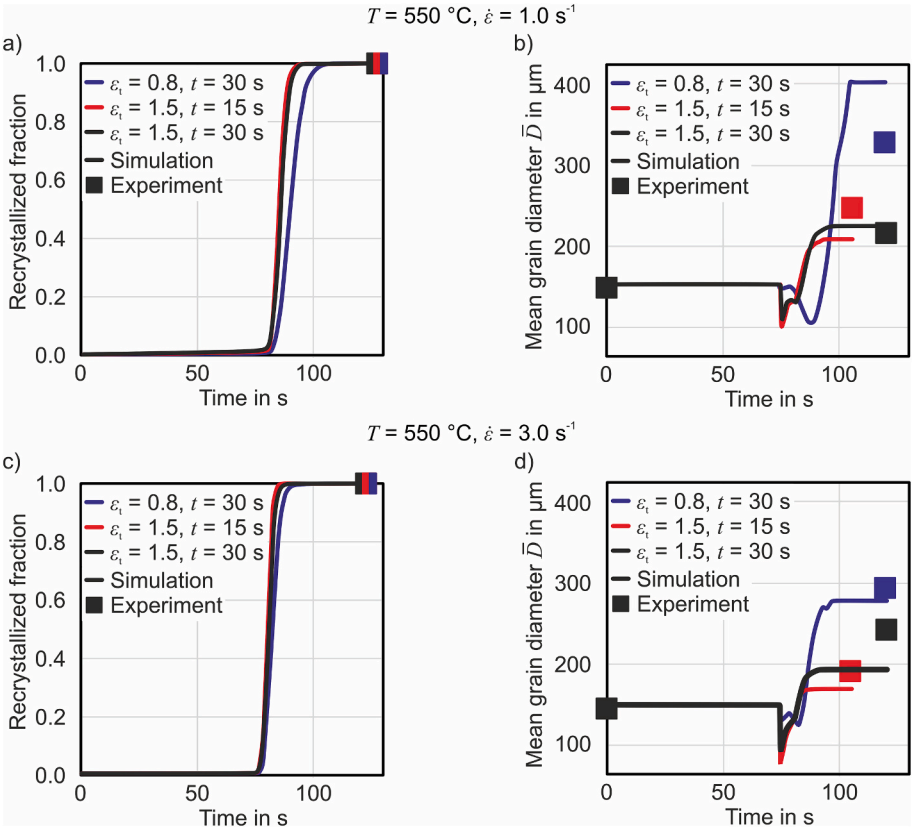

Fig. 10. Exemplary evolution of recrystallized fraction (a, c) and average grain size (b, d) calculated with the mean-field microstructure model for hot upsetting of AA6060 at 550 °C for $\dot{\varepsilon} = 1.0\ s^{-1}$ (a, b) and $\dot{\varepsilon} = 3.0\ s^{-1}$ (c, d).

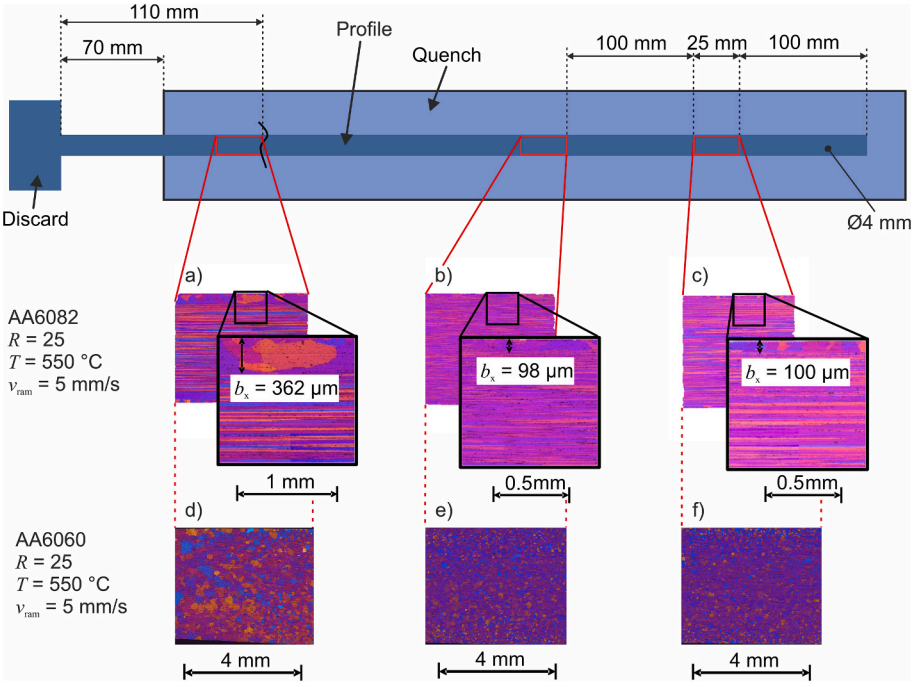

Fig. 11. Resulting microstructure of AA6060 (d-f) and AA6082 (a-c) depending on the position along the extrusion axis over the complete profile width.

towards the die, a more inhomogeneous microstructure regarding the grain size as well as the recrystallized fraction can be observed. This is due to the heat flux from the die and container into the profile. Therefore, the evaluation of the microstructure is done at a fixed distance of 100 mm from the beginning of the profile. A similar observation applies to small extrusion ratios. The lower achievable profile lengths of 220 mm for extrusion ratios of $R = 11.11$, compared to 500 mm at $R = 25$ and 880 mm at $R = 44.44$, prevents the development of steady-state

conditions in the extrusion process, and are therefore not used for the modeling or validation.

The extruded specimens of AA6060 show a strong tendency to recrystallize. Even at lower billet temperatures (in comparison to the upsetting tests) of 420 °C ($R = 25$, $v_{ram} = 5$ mm/s), recrystallized grains with an increase in size towards the center of the profile cross section can be observed. Increasing the billet temperature to 550 °C, or the extrusion ratio to $R = 44.44$, achieves complete recrystallization across the profile cross section. Moreover, a finer grain size is observed in the edge area, whereas the grain size is coarser in the center of the profile. The average grain length l_{ag} and resulting microstructure for different parameters are shown in Fig. 12.

As before, the predicted microstructures based on the strain and temperature histories of selected material points in the profiles obtained as described in Section 2.6 are compared to the experimentally-observed microstructures. As an example, Fig. 13 shows the results for two tests at 550 °C with a ram speed of 9 mm/s with two different extrusion ratios. Similar dependencies of the resulting microstructure on the position in the cross-section and process parameters like in the experiments are predicted by the recrystallization model. In particular, the conditions under which recrystallization does or does not occur are predicted accurately for all experimentally tested process parameter combinations (Fig. 13a and c). However, the contrast between the calculated grain sizes in the profile center and at its surface is not as strong as experimentally observed, as Fig. 13b and d illustrate. This indicates that the prediction of the final grain size is more sensitive to the input data than the prediction of the recrystallization state. Therefore, both the microstructure model and the input data from the process simulation may need further improvement. Despite these limitations, the prediction of the recrystallization state is highly accurate and the most robust output of the model. Consequently, the microstructure model for AA6060 can be regarded as satisfactorily validated.

With the calibrated and validated model, fictitious trials were calculated to further analyze the model behavior for AA6060. A total of 46,046 synthetic trials are calculated varying temperature (420 °C–600 °C and constant during the test), plastic strain (0.01–10), and strain-rate (1 s^{-1}–1000 s^{-1}). As a key result of this data set, combinations of process parameters that lead to recrystallization during the holding time after deformation can be separated from those combinations that do not induce recrystallization, as shown in Fig. 14. For various temperatures, a line highlights the strain-rate- and strain-dependent border between the recrystallization regime (top right portion) and the non-recrystallization regime (bottom left portion). As expected, a minimum strain-rate and minimum total strain is needed for recrystallization to set in. Up to approx. 500 °C, the strain-rate and total strain required for recrystallization decrease with increasing temperature. Above 500 °C, this trend is reverted due to the increasing importance of recovery effects, such that with further increasing temperature, increasing strain-rate and total strain are required for recrystallization to set in. With the information of Fig. 14 the recrystallization behavior of extrusion processes can be evaluated. By comparing the strain, strain-rate and temperature history of a material point with the depicted recrystallisation limits, the recrystallizing locations can be determined. Furthermore, to assure the occurrence of recrystallization either a variation of the temperature or the strain-rate in form of the ram speed can be enough to achieve a complete recrystallization.

3.5. Microstructural evolution model calibration for AA6082 with miniature extrusion

Since the hot upsetting tests of the alloy AA6082 show no signs of recrystallization of the microstructure (as seen in Section 3.2) due to the relatively low achievable strains ($\varepsilon_t = 1.5$) and strain-rates of not more than $\dot{\varepsilon} = 3\ s^{-1}$, the calibration of the recrystallization parameters of the microstructure model is not possible in this way. The aforementioned miniature extrusion trials achieved comparable critical thermo-mechanical conditions as in industrial extrusion to reach a recrystallization regime due to the higher total strain (maximum plastic strain of 6.7 – 9 for the investigated extrusion ratios $R = 25$ – 44.44) and strain-rates (locally exceeding 100 s^{-1}). In agreement to the results of the

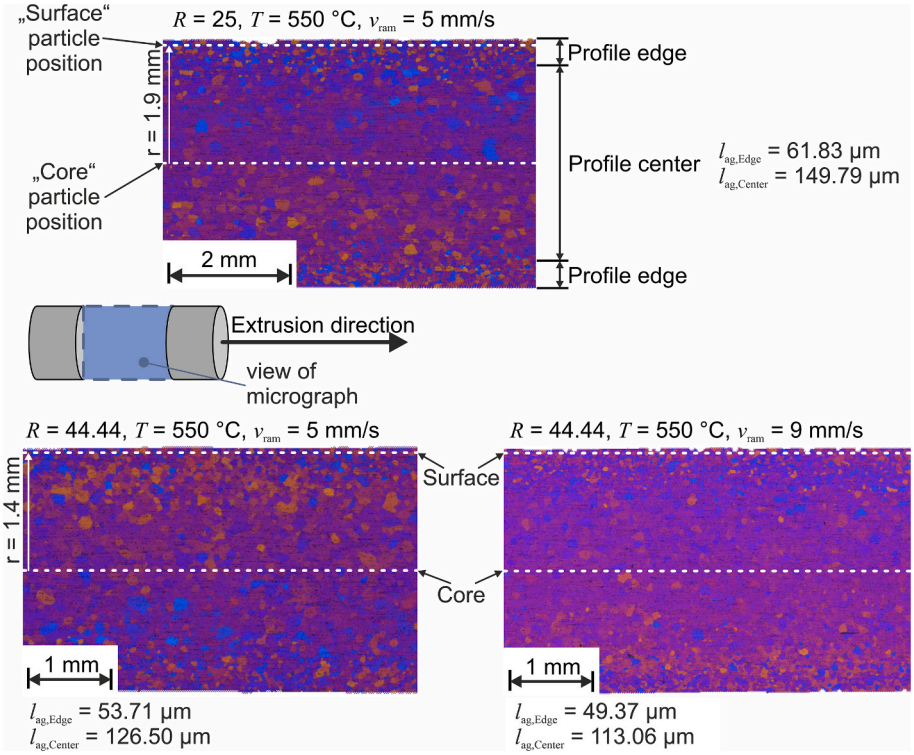

Fig. 12. Exemplary resulting recrystallized microstructures and average grain sizes of AA6060 after miniature extrusion at 550 °C with different extrusion ratios and ram velocities. The blue box in the schematic shows the plane of the microstructure images and is of the same size as the micrographs.

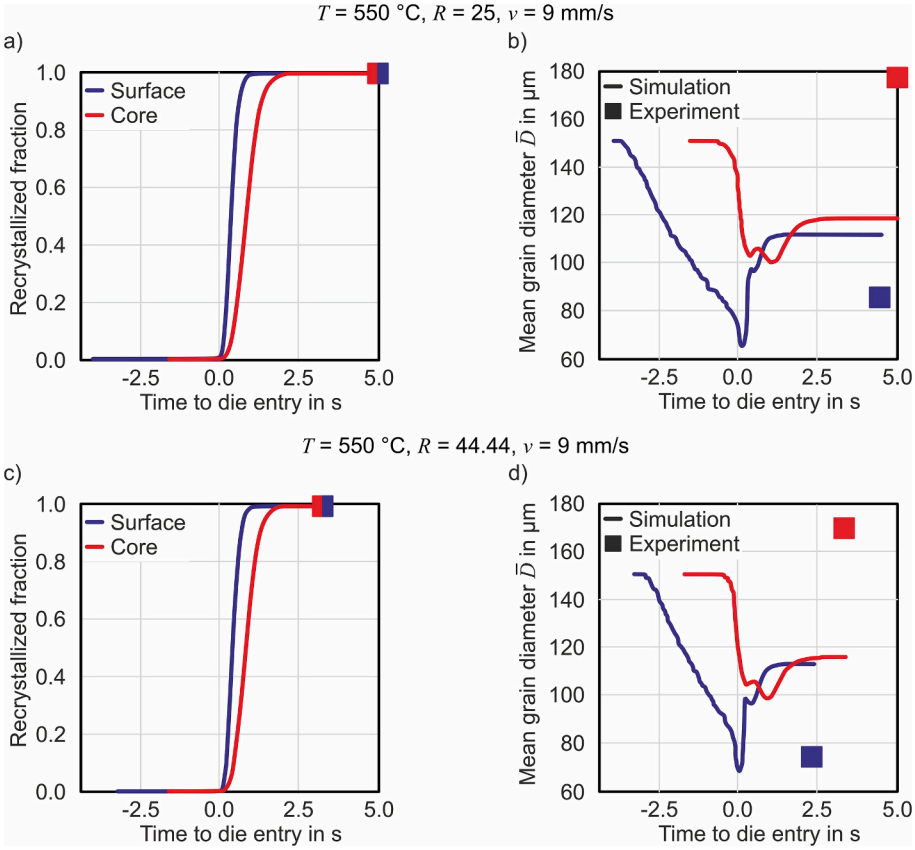

Fig. 13. Exemplary calculated evolution of recrystallized fraction (a,c) and average grain size (b,d) during miniature extrusion of AA6060 at 550 °C, ram velocity of 9 mm/s, and extrusion ratios $R = 25$ (a-b) and $R = 44.44$ (c-d).

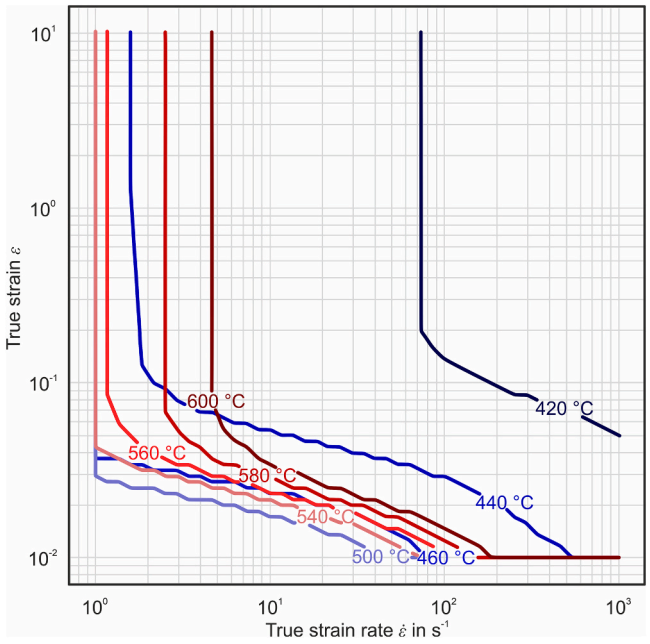

Fig. 14. Recrystallization process map for AA6060 calculated from synthetic data. For each temperature, the border separating the recrystallization regime (top right portion) and the non-recrystallization regime (bottom left portion) is drawn.

upsetting tests (Section 3.2), the lower tendency of AA6082 to recrystallize could also been seen during miniature extrusion. For this alloy, the resulting microstructural evolution can be divided into two cases:

- No recrystallization or nucleation of the microstructure. Only a strong elongation of the grains, leading to a fibrous microstructure.
- Recrystallization in the outer edge area of the profile. A fibrous microstructure, without recrystallization, remains at the core of the profile.

Fig. 15 shows the microstructure and the recrystallized fractions across the profile cross section for different parameter combinations. An extrusion ratio of $R = 25$ resulting in a total maximum plastic strain of 6.7 at $T = 450$ °C (Fig. 15a) is enough to achieve a fine recrystallized edge area with a thickness of 13.43 µm. With the increase of the temperature to 550 °C (Fig. 15b) the thickness of the recrystallized edge area can be increased by 373 % to 63.59 µm. A further growth of the edge area thickness of up to 95.14 µm (+50 %) and 80.58 µm (+27 %), respectively Fig. 15c and Fig. 15d, can be observed by increasing the extrusion ratio to 44.44. The smaller edge area for the higher ram speed of 9 mm/s can be explained by the resulting time between tool and quench. At a speed of 5 mm/s the extrudates remains at a high temperature for 0.32 s before it reaches the quench. At a ram speed of 9 mm/s, the time interval for grain growth is only 0.18 s before the resulting microstructure is frozen by the quench. Additional extrusion trials with a billet temperature of 600 °C did not cause any recrystallization or nucleation of the microstructure comparable to the results of the fictitious trials of AA6060, needing a higher amount of total strain and/or strain-rate to achieve a recrystallization regime.

The calibration of the material parameters for the microstructure model for AA6082 is done in accordance to Section 3.3 and results in a

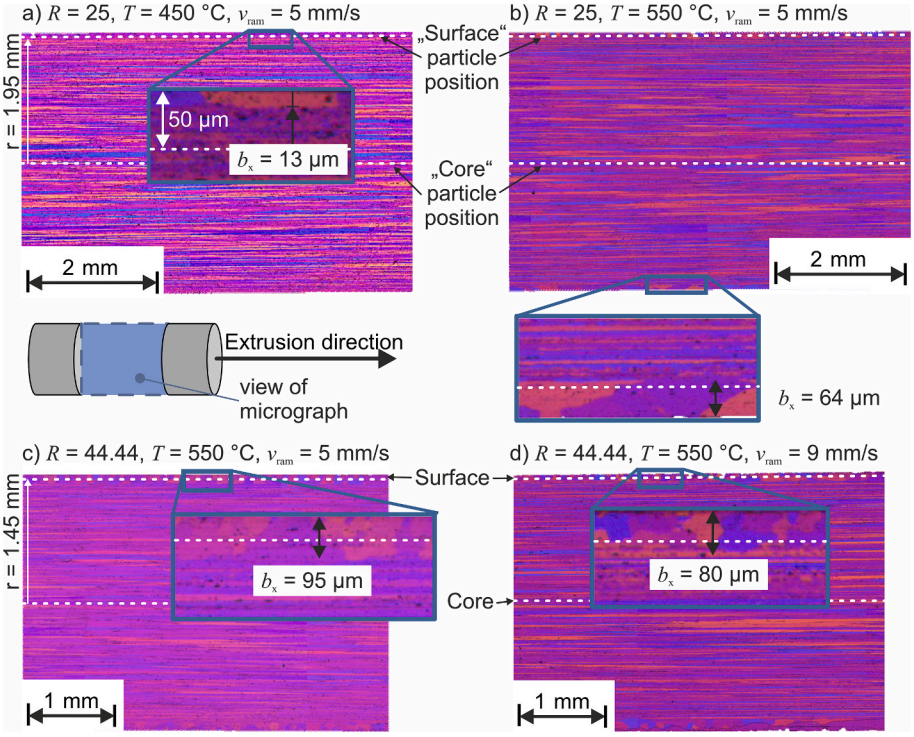

Fig. 15. Exemplary resulting microstructures of miniature extruded AA6082 showing no recrystallization in the investigated material point "surface" at lower temperature (a) or a recrystallized edge zone (b-d) with varying thickness due to the different process parameters listed in the micrographs.

similar predictive accuracy as for AA6060. For the recrystallization parameters, the strain and temperature histories of the miniature extrusion trials are calculated on five positions along the radius of the profiles as described in Section 2.6 and are used as input to the model. The predicted microstructures are compared to the experimentally obtained ones from the miniature extrusion trials. The model parameters are iteratively adapted in order to achieve the best possible agreement between experiment and simulation (Table 6). Since this calibration is conducted through experimental and numerical extrusion trials, it had to be calibrated with significantly more assumptions or under consideration of complex boundary conditions. As a result, the prediction accuracy is lower compared to that of AA6060, which was calibrated with hot upsetting tests. Nonetheless, the validation in Section 3.6 demonstrates the robustness of the calibrated model in predicting whether a material point ends up in a recrystallized state and suggest that miniature extrusion trials are a suitable alternative for calibration.

Table 6
Parameters of the microstructural evolution model for AA6082. R_{gas} denotes the gas constant and T the absolute temperature.

	AA6082
μ in GPa	$26\left(1-0.2\frac{T-300\,\mathrm{K}}{600\,\mathrm{K}}\right)$
ξ^1	0.0273
β^1	$119657\exp\left(-\frac{43\,\mathrm{kJ/mol{\cdot}K}}{R_{gas}\cdot T}\right)$
x^1	0
ξ^2	0.6760
β^2	$9250.08\exp\left(-\frac{17\,\mathrm{kJ/mol{\cdot}K}}{R_{gas}\cdot T}\right)$
x^2	0.1822
$a^1 = a^2$ in s^{-1}	$0.3\exp\left(-\frac{20\,\mathrm{kJ/mol{\cdot}K}}{R_{gas}\cdot T}\right)$
M_{gb} in $\frac{m^4}{J\bullet s}$	$2{\cdot}10^{-2}\exp\left(-\frac{98\,\mathrm{kJ/mol{\cdot}K}}{R_{gas}\cdot T}\right)$
σ_{gb} in $\frac{J}{m^2}$	0
A in s^{-1}	$10^{26}\exp\left(-\frac{274\,\mathrm{kJ/mol{\cdot}K}}{R_{gas}\cdot T}\right)$
φ_1	0.002
φ_2	$27.8\exp\left(-\frac{20\,\mathrm{kJ/mol{\cdot}K}}{R_{gas}\cdot T}\right)$
$\psi_{p,cr}$ in $\frac{J}{m^3}$	$2.4{\cdot}10^8\left(1+\tanh\left(17.76-0.0300\frac{T}{K}\right)\right)+4.4{\cdot}10^4$
R_0 in µm	1
k_0 in MPa	$7.40\left(1-0,50\frac{T-723\,\mathrm{K}}{100\,\mathrm{K}}\right)$

3.6. Validation with industrially-scaled trials for AA6082

For the validation of the calibrated microstructure model for AA6082 industrially-scaled extrusion trials are conducted. A typical double-chamber profile (Fig. 16a) in a parallel 2-profile set up (Fig. 16b) with an extrusion ratio $R = 20$ and industrial process parameters used for production ($T = 480$ °C, $v_{ram} = 4.51$ mm/s, water spray mist quench) are chosen.

With the different wall thicknesses and an inner profile bridge without direct contact to the quenching medium, different conditions with regard to the resulting microstructure across the profile cross section can be observed (Fig. 17). The observed microstructure is comparable to the microstructure after miniature extrusion, showing a completely recrystallized edge area of one to two grains in thickness and a fibrous, non-recrystallized center structure.

The four shown areas of the profile cross section (inner and outer longitudinal weld seam area, upper and middle bridge) are chosen and the material model is applied to five material points equally distributed through the wall thickness (as discussed in Section 2.6). For the calculation of the input data for the material model, a numerical simulation of the industrial extrusion trial was set up in agreement to Section 2.6 and was also validated with the ram force (maximum ram force in experiment: 21.6 MN, in simulation: 20.3 MN). The model is able to successfully predict whether a particle path ends in a recrystallized microstructure or not for all these investigated material points.

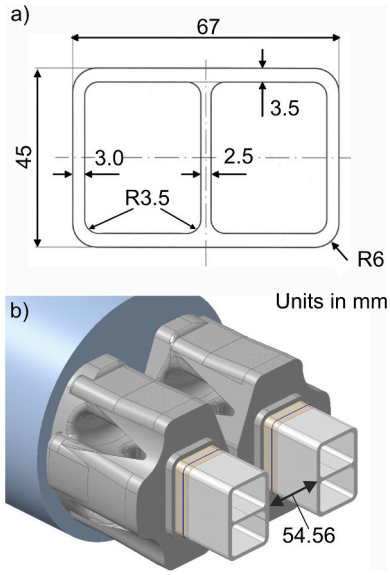

Fig. 16. a) cross section of the industrial profile b) flow volume inside the die and two-profile setup of the industrial profile for validation of the microstructural evolution model.

Considering the complex process of hot extrusion of hollow profiles, the experimental and predicted average grain sizes in the recrystallized areas are generally in good agreement (Fig. 18). Depending on the location of the points along the profile cross-section, the agreement ranges from excellent to average. For example, in the recrystallized edge area on the outside of the upper bridge the average grain size measures 146 μm and the model prediction is 137 μm, resulting in a deviation of 6.1 %. Overall, the average grain size is predicted within 20 % of the measured value in recrystallized areas on the outside of the profile (blue bars in Fig. 18).

On the other hand, the predicted grain sizes of the inner edges of the profile tend to be underestimated in the simulations by up to 100 μm. For example, on the inner side of the outer longitudinal weld seam the average grain size after extrusion is 196 μm, where as the model predicts 93 μm. This can be partially attributed to the incomplete modeling of the quenching process after forming, since the extensive spray mist quench cannot be fully represented numerically. Instead, exemplary expected cooling rates from the industry between 20–180 K/s are used in the microstructural model, i.e., 180 K/s for material points at the outside of the profile and 20 K/s for material points on the inside of the middle bridge. The cooling rate is an average value determined by the measured temperature difference of the extrudate between entering and leaving the quench and was given by the industrial consortium of this project. In the industrial trial, this could not be validated for different positions, especially on the inside of the profile. The investigated results suggest that for a more precise prediction of the recrystallized grain size, detailed data of the quenching process is needed. An exception from the overall underestimation of the predicted average grain size is the outside area of the inner longitudinal weld seam. A possible explanation could be the radiative heat transfer from the second profile extruded parallel to each other, which is overestimated in the simulations.

4. Summary and Conclusions

A workflow to numerically predict the recrystallization behavior during hot extrusion was implemented as a post-processing method with a mean-field microstructure model newly introduced to the process of

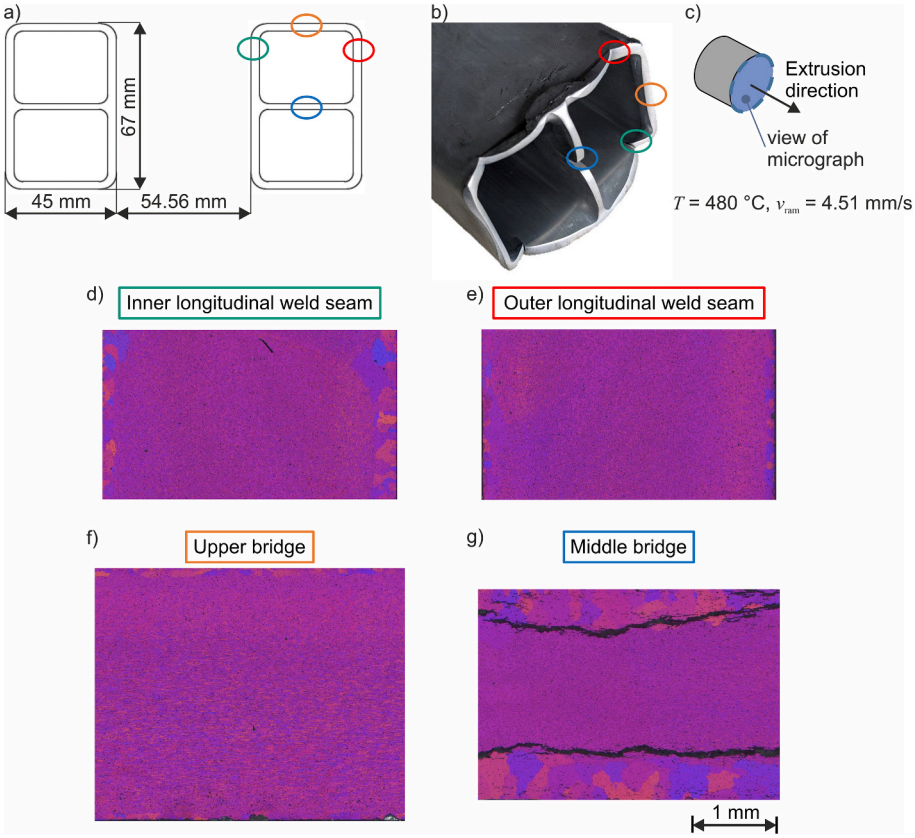

Fig. 17. a) investigated areas of the industry profile in regards to the position of the two strand extrusion. b) beginning of the profile with visible positions of the weld seams. d-g) resulting microstructure of the extruded industry profile of AA6082 at 480 °C and ram speed 4.51 mm/s after quenching. The blue circle in the schematic c) indicates the plane of the microstructure images in regards to the extrusion direction.

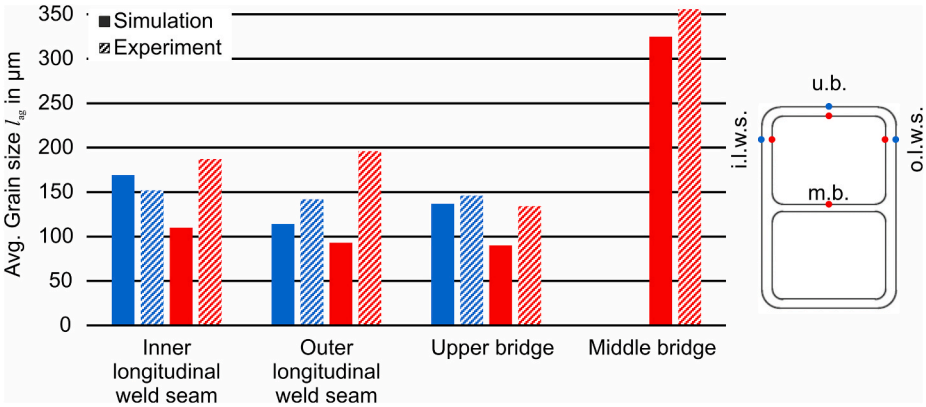

Fig. 18. Comparison of the calculated and measured average grain sizes at different position of the profile cross section where recrystallization could be observed at a billet temperature of 480 °C and ram speed of 4.51 mm/s for AA6082. The average grain size in the as-received billet is 93.4 µm.

aluminum profile extrusion. Furthermore, a new setup for calibration and parameter identification was introduced. The model was calibrated for the aluminum alloys AA6060 and AA6082. The key findings are summarized as follows:

- The mean-field model can reliably predict the profile areas in which recrystallization will occur for AA6060 and AA6082 and was validated by both the miniature/laboratory- and industrial-scale trials.
- The predicted grain size is in reasonable agreement with the experimental results. For the directly quenched outer areas of the profile, the predicted average grain size deviates from the experiments between 7–20 %. The investigated outside area between the two profile strands show a deviation of 11 %. Whereas, the predicted grain size in the recrystallized edge area on the inside of profile deviates between 8–52 % from the experimental results. Further analysis of the needed accuracy of the input data and the influence of small deviations of those are required, as well as a more detailed analysis of the local cooling rates.
- The average grain size was used to determine the accuracy of the prediction. However, with the mean-field model it is possible to further calculate the grain size distribution, which is planned for further investigations.
- The presented workflow and the underlying physics-based modelling framework are fundamentally applicable to other aluminum alloy systems, such as the 2xxx or 7xxx series. The material-specific parameters (e.g. for plasticity, recovery and nucleation) would need to be completely re-characterized and re-calibrated for each new alloy, and a more complex precipitation model (e.g. for multiple phases) may also be required.

Declaration of generative AI and AI-assisted technologies in the writing process

During the preparation of this work the authors used Microsoft Copilot in order to improve the readability and language of the manuscript. After using this tool, the authors reviewed and edited the content as needed and take full responsibility for the content of the published article.

CRediT authorship contribution statement

Oliver Schulz: Writing – review & editing, Writing – original draft, Visualization, Validation, Software, Methodology, Investigation, Formal analysis, Data curation. **Lukas Kertsch:** Writing – review & editing, Writing – original draft, Visualization, Validation, Software, Methodology, Investigation. **Johannes Gebhard:** Writing – review & editing, Supervision, Project administration, Conceptualization. **Yannis P. Korkolis:** Writing – review & editing, Supervision, Resources, Project administration, Methodology, Investigation, Funding acquisition, Conceptualization. **A. Erman Tekkaya:** Writing – review & editing, Supervision, Resources, Project administration, Methodology, Investigation, Funding acquisition, Conceptualization. **Maksim Zapara:** Supervision, Project administration, Funding acquisition, Conceptualization.

Declaration of competing interest

The authors declare that they have no known competing financial interests or personal relationships that could have appeared to influence the work reported in this paper.

Acknowledgments

This study was funded by the Federal Ministry for Economic Affairs and Climate Action on the basis of a resolution of the German Bundestag (IGF: 21682 N).

A. Appendix.

.

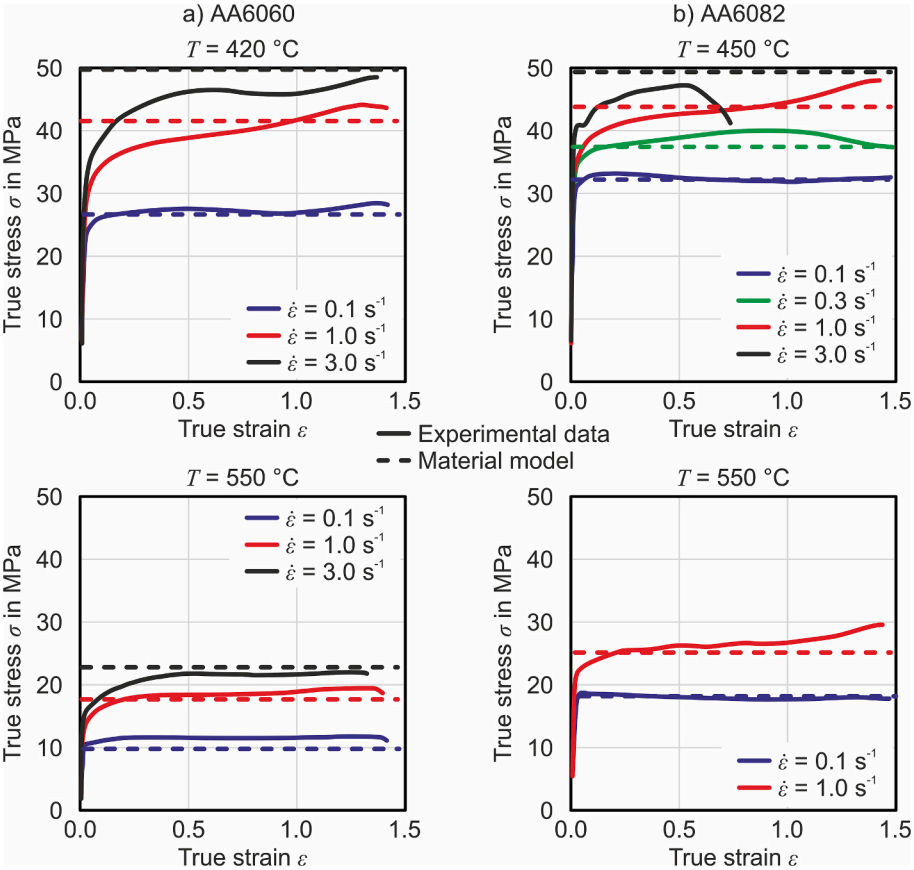

Fig. A1. Comparison between experimental flow curves and the flow stress from the material model used in Inspire Extrude for a) AA6060 (left side) at 420 °C and 550 °C and various strain-rates and b) the adapted AA6082 (right side) at 450 °C and 550 °C and various strain-rates.

.

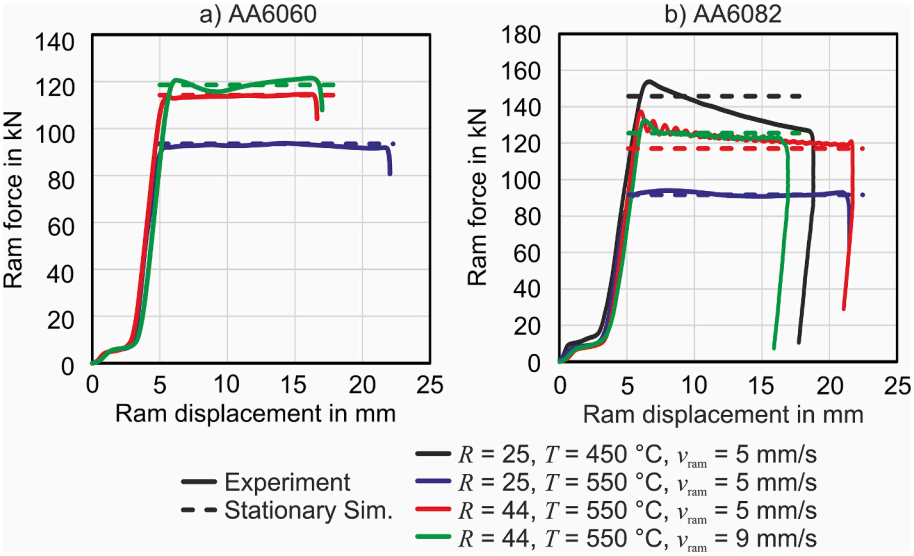

Fig. A2. Validation of the simulations of the steady state via the force displacement curves of the miniature extrusion trials for different process parameters with a) AA6060 and b) AA6082.

Data availability

Data will be made available on request.

References

[1] M. Bauser (Ed.), Extrusion, 2nd ed., ASM International, Materials Park, Ohio, 2006.
[2] W.H. van Geertruyden, H.M. Browne, W.Z. Misiolek, P.T. Wang, Evolution of surface recrystallization during indirect extrusion of 6xxx aluminum alloys, Metall. Mater. Trans. A 36 (4) (2005) 1049–1056, https://doi.org/10.1007/s11661-005-0298-6.

[3] S.-W. Bai, G. Fang, J. Zhou, Analysis of the bonding strength and microstructure of AA6082 extrusion weld seams formed during physical simulation, J. Mater. Process. Technol. 250 (2017) 109–120, https://doi.org/10.1016/j.jmatprotec.2017.07.012.
[4] G. Drossel, S. Friedrich, W. Huppatz, C. Kammer, W. Lehnert, O. Liesenberg, et al., Aluminium-Taschenbuch, 17th ed., Beuth Verlag GmbH, Berlin, Wien, Zürich, 2018.
[5] G.-z. Quan, Y.-p. Mao, G.-s. Li, W.-q. Lv, Y. Wang, J. Zhou, A characterization for the dynamic recrystallization kinetics of as-extruded 7075 aluminum alloy based on true stress–strain curves, Comput. Mater. Sci 55 (2012) 65–72, https://doi.org/10.1016/j.commatsci.2011.11.031.
[6] X. Zhang, F. Ma, W. Zhang, X. Li, Kinetics of dynamic recrystallization in AA2024 aluminum alloy, MAS 8 (6) (2014), https://doi.org/10.5539/mas.v8n6p47.
[7] H.E. Hu, L. Zhen, B.Y. Zhang, L. Yang, J.Z. Chen, Microstructure characterization of 7050 aluminum alloy during dynamic recrystallization and dynamic recovery, Mater Charact. 59 (9) (2008) 1185–1189, https://doi.org/10.1016/j.matchar.2007.09.010.
[8] H.J. McQueen, O. Knustad, N. Ryum, J.K. Solberg, Microstructural evolution in Al deformed to strains of 60 at 400°C, Scr. Metall. 19 (1) (1985) 73–78, https://doi.org/10.1016/0036-9748(85)90268-6.
[9] A. Güzel, A. Jäger, F. Parvizian, H.-G. Lambers, A.E. Tekkaya, B. Svendsen, et al., A new method for determining dynamic grain structure evolution during hot aluminum extrusion, J. Mater. Process. Technol. 212 (1) (2012) 323–330, https://doi.org/10.1016/j.jmatprotec.2011.09.018.
[10] R.A. Jeniski, B. Thanaboonsombut, T.H. Sanders, The effect of iron and manganese on the recrystallization behavior of hotrolled and solution-heat-treated aluminum alloy 6013, Metall. Mater. Trans. A 27 (1) (1996) 19–27, https://doi.org/10.1007/BF02647743.
[11] C. Li, K. Liu, X.-G. Chen, Improvement of elevated-temperature strength and recrystallization resistance via Mn-containing dispersoid strengthening in Al-Mg-Si 6082 alloys, J. Mater. Sci. Technol. 39 (2020) 135–143, https://doi.org/10.1016/j.jmst.2019.08.027.
[12] F. Birchall, C. Bishop, High-Throughput quantification of recrystallization parameters for alloy development, Metall. Mater. Trans. A 5 (2025) 717, https://doi.org/10.1007/s11661-025-07822-4.
[13] L. de Pari, W.Z. Misiolek, Theoretical predictions and experimental verification of surface grain structure evolution for AA6061 during hot rolling, Acta Mater. 56 (20) (2008) 6174–6185, https://doi.org/10.1016/j.actamat.2008.08.050.
[14] A. Foydl, A. Segatori, N.B. Khalifa, L. Donati, A. Brosius, L. Tomesani, et al., Grain size evolution simulation in aluminium alloys AA 6082 and AA 7020 during hot forward extrusion process, Mater. Sci. Technol. 29 (1) (2013) 100–110, https://doi.org/10.1179/1743284712Y.0000000132.
[15] S.F. Chen, D.Y. Li, S.H. Zhang, H.N. Han, H.W. Lee, M.G. Lee, Modelling continuous dynamic recrystallization of aluminum alloys based on the polycrystal plasticity approach, Int. J. Plast 131 (2020) 102710, https://doi.org/10.1016/j.ijplas.2020.102710.
[16] T. Manik, K. Marthinsen, K. Zhang, A.I. Aria, B. Holmedal, Deformation texture evolution in flat profile AlMgSi extrusions: experiments, FEM, and crystal plasticity modeling, Front. Mater. 8 (2021) 111, https://doi.org/10.3389/fmats.2021.636379.
[17] M. Knezevic, R.J. McCabe, R.A. Lebensohn, C.N. Tomé, C. Liu, M.L. Lovato, et al., Integration of self-consistent polycrystal plasticity with dislocation density based hardening laws within an implicit finite element framework: Application to low-symmetry metals, J. Mech. Phys. Solids 61 (10) (2013) 2034–2046, https://doi.org/10.1016/j.jmps.2013.05.005.
[18] M. Knezevic, M. Jahedi, Y.P. Korkolis, I.J. Beyerlein, Material-based design of the extrusion of bimetallic tubes, Comput. Mater. Sci 95 (2014) 63–73, https://doi.org/10.1016/j.commatsci.2014.07.021.
[19] I.A. Riyad, M. Knezevic, Predicting the evolution of texture and grain size during deformation and recrystallization of polycrystals using field fluctuations viscoplastic self-consistent crystal plasticity, Mech. Mater. (2024) 105212, https://doi.org/10.1016/j.mechmat.2024.105212.
[20] Z. Cheng, C. Zhang, G. Chu, Z. Liu, K. Wang, Z. Meng, et al., Dynamic precipitation and recrystallization behavior during hot deformation of Al-Zn-Mg-Cu alloy: Experiment and modeling, Int. J. Plast. 178 (2024) 103995, https://doi.org/10.1016/j.ijplas.2024.103995.
[21] X. Liu, J. Zhu, Y. He, H. Jia, B. Li, G. Fang, State-of-the-Art review of the simulation of dynamic recrystallization, Metals 14 (11) (2024) 1230, https://doi.org/10.3390/met14111230.
[22] H. Riedel, J. Svoboda, A model for strain hardening, recovery, recrystallization and grain growth with applications to forming processes of nickel base alloys, Mater. Sci. Eng. A 665 (2016) 175–183, https://doi.org/10.1016/j.msea.2016.04.015.
[23] M. Roth, B. Flipon, N. Bozzolo, M. Bernacki, Comparison of grain-growth mean-field models regarding predicted grain size distributions, Materials (basel) 16 (20) (2023), https://doi.org/10.3390/ma16206761.
[24] M.-I.-T. Tzini, G.N. Haidemenopoulos, A physically based mean field model for strain-induced precipitation and recrystallization in high-strength low-alloy steels, Steel Research Int. 96 (1) (2025) 493, https://doi.org/10.1002/srin.202400493.
[25] R.S. Subramanian, R.S. Shree, P.G.K. Amos, Analyzing and extending cellular automaton simulations of dynamic recrystallization, ComplexSystems 32 (2) (2023) 189–209, https://doi.org/10.25088/ComplexSystems.32.2.189.
[26] A. Rezvani, R. Ebrahimi, E. Bagherpour, Static recrystallization simulation of interstitial free-steel by coupling multi-phase-field and crystal plasticity model considering dislocation density distribution, Adv. Eng. Mater. 27 (12) (2025) 416, https://doi.org/10.1002/adem.202500117.
[27] H. Xu, X. Shu, J. Zuo, A. Yin, Y. Wang, Kinetic monte carlo simulation of abnormal grain growth in textured systems with anisotropic grain boundary energy and mobility, Mater. Today Commun. 30 (10) (2022) 103133, https://doi.org/10.1016/j.mtcomm.2022.103133.
[28] B. Scholtes, M. Shakoor, A. Settefrati, P.-O. Bouchard, N. Bozzolo, M. Bernacki, New finite element developments for the full field modeling of microstructural evolutions using the level-set method, Comput. Mater. Sci 109 (2015) 388–398, https://doi.org/10.1016/j.commatsci.2015.07.042.
[29] L. Kertsch, D. Helm, A thermodynamically consistent model for elastoplasticity, recovery, recrystallization and grain coarsening, Int. J. Solids Struct. 152–153 (2018) 185–195, https://doi.org/10.1016/j.ijsolstr.2018.06.026.
[30] L. Kertsch, Modellierung des thermomechanischen Materialverhaltens und der Gefügeentwicklung mikrolegierter Stähle [Dissertation]: Karlsruher Institut für Technologie, Fraunhofer IRB-Verlag, Fraunhofer-Institut für Werkstoffmechanik IWM, 2022.
[31] M. Hillert, On the theory of normal and abnormal grain growth, Acta Metall. 13 (3) (1965) 227–238, https://doi.org/10.1016/0001-6160(65)90200-2.
[32] F.D. Fischer, J. Svoboda, P. Fratzl, A thermodynamic approach to grain growth and coarsening, Phil. Mag. 83 (9) (2003) 1075–1093, https://doi.org/10.1080/0141861031000068966.
[33] D.G. Cram, H.S. Zurob, Y.J.M. Brechet, C.R. Hutchinson, Modelling discontinuous dynamic recrystallization using a physically based model for nucleation, Acta Mater. 57 (17) (2009) 5218–5228, https://doi.org/10.1016/j.actamat.2009.07.024.
[34] P. Bernard, S. Bag, K. Huang, R.E. Logé, A two-site mean field model of discontinuous dynamic recrystallization, Mater. Sci. Eng. A 528 (24) (2011) 7357–7367, https://doi.org/10.1016/j.msea.2011.06.023.
[35] E.E. Underwood, Quantitative stereology, Addison-Wesley Publishing Company, Reading, Mass, 1970.
[36] C. Zener, J.H. Hollomon, Effect of strain rate upon plastic flow of steel, J. Appl. Phys. 15 (1) (1944) 22–32, https://doi.org/10.1063/1.1707363.
[37] C.M. Sellars, W.J.M. Tegart, Hot workability, Int. Metall. Rev. 17 (1) (1972) 1–24, https://doi.org/10.1179/imtlr.1972.17.1.1.
[38] H.S. Valberg, Analysis of metal flow of aluminum through long choked die channels, KEM 424 (2009) 145–152, https://doi.org/10.4028/www.scientific.net/KEM.424.145.
[39] M. Negozio, R. Pelaccia, L. Donati, B. Reggiani, L. Tomesani, T. Pinter, FEM validation of front end and back end defects evolution in AA6063 and AA6082 aluminum alloys profiles, Procedia Manuf. 47 (6) (2020) 202–208, https://doi.org/10.1016/j.promfg.2020.04.178.
[40] F.J. Humphreys, M. Hatherly, Recrystallization and related annealing phenomena, 2nd ed., Elsevier, Amsterdam, Heidelberg, 2004.